

Differential Depletion-Induced 3D Stress Modification in Fault-Bounded Reservoirs and Implications for Fault Stability in Three Faulting Regimes

Lei Jin¹

¹Department of Geophysics, Stanford University, California 94305

Corresponding author: Lei Jin (leijin@alumni.stanford.edu)

Abstract

Depletion-induced faulting has been documented in a number of hydrocarbon reservoirs. This type of faulting has mostly been attributed to poroelastic effects: in-situ horizontal stresses are coupled with a pore pressure change according to a certain coupling coefficient (known as the stress path), which is generally less than 1. For faults with certain orientations, if the stress path is sufficiently high, the shear stress and effective normal stress resolved on the fault increase in such a manner that the fault is brought towards the shear failure line. An underlying assumption associated with this mechanism is that homogeneous pore pressure depletion occurs on both sides of the fault.

This study addresses an additional mechanism for depletion-induced faulting in cases where the pore pressure reduction is bounded by a hydraulically impermeable fault. Unbalanced pore pressure changes on the two sides of the fault, in conjunction with the poroelastic response, cause redistribution of the stress state. Two key assumptions are made: (1) pore pressure depletion is homogeneous within the reservoir on one side of the impermeable fault, and (2) the overburden stress and shear stresses are decoupled from pore pressure, while the two horizontal principal stresses are coupled with pore pressure by their respective stress paths (we show that the poroelastic coupling effect is anisotropic). Given a fault that is arbitrarily oriented with respect to the original stress field, we derive a generalized 3D analytical solution for the new state of stress after depletion. We then quantify the change in magnitude and rotation of the three principal stresses. Finally, we compare the corresponding Coulomb Failure Functions and Mohr Circles before and after depletion. For demonstration purposes, we determine the stress path tensor using poroelastic plane strain solutions in conjunction with frictional equilibrium for three different faulting regimes. Our hypothetical case studies show that, for bounded reservoirs, depletion-induced principal stress rotation and magnitude changes have a significant impact on fault stability, and are a complex function of fault orientation, the original in-situ stress state and pore pressure, the degree of depletion, and the degree of poroelastic coupling.

1. Introduction

The stress state within a reservoir is coupled to pore pressure changes resulting from fluid injection and withdrawal. The most commonly observed coupling is between the least horizontal principal stress and pore pressure. The coupling coefficient, dS_{hmin}/dP_p , is commonly known as the stress path. The stress path associated with depletion at reservoir scales ranges

from 0.34 to 1.18 (Addis,1997; Hillis, 2000; Altmann et al., 2010), and is between 0.6 and 0.8 for over-pressured compartments at basin scales (Engelder and Fischer,1994; Hillis,2001; Tingay et al., 2003). Coupling between maximum horizontal principal stress and pore pressure is predicted but has rarely been reported in the field due to difficulties in measuring the relationship. Overburden and shear stresses are generally assumed to be de-coupled from pore pressure changes.

One particularly interesting coupling phenomenon is the rotation of principal stresses due to stress-pore pressure coupling effects, which has been documented in a number of studies. Mourgues and Cobbold (2003) demonstrated via sandbox experiments that a fluid overpressure gradient induces seepage forces, which act as additional stress components, modify the total stress tensor, and induce principal stress rotations. Such rotations have also been revealed by stress inversion techniques using focal mechanisms of fluid injection-induced and depletion-induced seismic events (Martínez-Garzón et al., 2013). In the case where the coupling effect is substantial, even the overall stress regime can be altered (Schoenball et al., 2014).

One challenge associated with studying fluid pressure-stress coupling and the resulting stress rotation is the determination of the coupling coefficient. While this coupling relation can be established empirically for specific sites (Aadnoy, 1991), it can also be predicted using a number of analytical models suitable for porous media; these models assume known stress regimes, boundary conditions, and reservoir geometries. One such model, the uniaxial strain model, is derived from Boit's theory of poroelasticity by prescribing zero lateral strain. This model gives a reasonable prediction for laterally extensive reservoirs under normal faulting regimes, and has been widely used for various purposes, including predicting in-situ stress (Van Ruth et al., 2003) and explaining production-induced normal faulting (Zoback and Zinke, 2002). The effects of material anisotropy can be incorporated into the uniaxial strain model (Addis, 1997). Frictional limit theory (Zoback et al., 2002) serves as another model for constraining stress paths, and is not limited to any specific stress regimes. These two models are parametrically and geometrically sensitive, and introduce uncertainties during work such as fault stability analysis (Vidal-Gilbert et al., 2009; Segura et al., 2011). A completely different approach is to use Eshelby inclusion theory (Eshelby, 1957) to derive the pore pressure change-induced stress perturbation within the reservoir to account for complex geometric effects (Segall & Fitzgerald, 1998) and to further construct stress paths under different geometric and parametric conditions (Rudnicki, 1999). Note that all of these models are associated with an important assumption: that pore pressure change is homogeneous within the reservoir. Thus, when using the coupling coefficients derived from these models to explain depletion-induced faulting, an underlying assumption is that pore pressure depletion occurs on both sides of the fault, and that depletion-induced faulting is a consequence of poroelastic effects only.

In this study, we incorporate depletion-induced principal stress rotations into fault stability analysis. This step is particularly important for a reservoir bounded by hydraulically impermeable faults. Unbalanced pore pressure changes on the two sides of the fault, in conjunction with poroelastic response, cause redistribution of the stresses to honor the traction boundary conditions across the fault.

We first derive a generalized 3D analytical solution for the new state of stress within a reservoir after depletion. We determine the stress paths for three stress regimes using poroelastic plane strain solutions in conjunction with frictional equilibrium theory. Then, we quantify changes in

the magnitude and orientation of the principal stresses through a number of hypothetical studies and show that including consideration of principal stress rotations can result in radically different predictions than those made based solely on poroelastic effects. These predictions are a complex function of fault orientation, the original in-situ stress state and pore pressure, the degree of depletion, and the degree of poroelastic coupling.

2. 3D Stress state after depletion without principal stress rotations

Let δp be the pore pressure change due to depletion ($\delta p < 0$). We make the following assumptions: (1) pore pressure change δp is homogeneous within the reservoir; (2) temporal effects are neglected; (3) S_v and shear stresses are decoupled from δp ; and (4) S_{hmin} and S_{Hmax} are coupled with pore pressure change by their respective stress paths A_h and A_H (in this study, the terms stress path and coupling coefficient are used interchangeably).

We define the stress path tensor as:

$$A_{ij} = \frac{\partial S_{ij}}{\partial p} \quad . \quad (1)$$

Based on the assumption above, A_{ij} is then:

$$A_{ij} = \begin{bmatrix} A_h & 0 & 0 \\ 0 & A_H & 0 \\ 0 & 0 & 0 \end{bmatrix} \quad , \quad (2)$$

where

$$A_h = \frac{\partial S_h}{\partial p} \quad , \quad (2.1)$$

$$A_H = \frac{\partial S_H}{\partial p} \quad . \quad (2.2)$$

So the new in-situ stress tensor after pore pressure change is:

Figure 1: Left: A 3D schematic model of a reservoir bounded by an impermeable fault. One-sided pore pressured depletion and anisotropic poroelastic response of the in-situ stresses require redistribution and re-equilibration of the stress state to honor the traction boundary condition across the fault. This equilibration causes changes in the magnitudes and rotations of principal stresses. Right: Old and new coordinates with respect to fault geometry and stress orientation.

3.2 New stress state within the reservoir after depletion and rotation of principal stresses

A 2D analytical solution is provided by Day-Lewis & Zoback (2007), who follow the approach of Sonder (1990); in this approach, the new stress state within the reservoir after depletion can be found by superimposing the uniaxial fault-normal stress perturbation onto the depleted background stress state (see Appendix A.1). This solution is derived graphically using a Mohr circle. The stress path is assumed to be the same for both S_{Hmin} and S_{Hmax} , meaning depletion is treated as isotropic, inducing no shear stress on the fault. In reality, this is generally not the case. To account for the anisotropy of the stress path, an alternative approach utilizing stress transformation is provided in Appendix A.2. This section generalizes the approach into 3D.

Compared to original stress state, the depletion induced additional loading in x - y - z is:

$$\Delta_{ij} = \begin{bmatrix} A_h \delta p & 0 & 0 \\ 0 & A_H \delta p & 0 \\ 0 & 0 & 0 \end{bmatrix} . \quad (6)$$

The associated traction resolved on the fault is then:

$$T_i = D_{ij} n_j = \left(A_h dp \sin d \cos f, -A_H dp \sin d \sin f, 0 \right)^T . \quad (7)$$

We choose a new coordinate system x' - y' - z' such that the fault plane is one of the orthogonal planes (see Figure 1), and let ex' , ey' and ez' be the directional cosines of the base vectors along x' , y' , and z' directions with respect to x , y and z :

$$\bar{e}_{x'} = \left(\cos \delta \cos \phi, -\cos \delta \sin \phi, -\sin \delta \right)^T , \quad (8.1)$$

$$\bar{e}_{y'} = \left(\sin \phi, \cos \phi, 0 \right)^T , \quad (8.2)$$

$$\vec{e}_{z'} = (\sin \delta \cos \phi, -\sin \delta \sin \phi, \cos \delta)^T = \vec{n} \quad . \quad (8.3)$$

Since the stress path is anisotropic, both normal and shear stresses will be induced by Δ_{ij} . In x' - y' - z' , they can be found by the dot product of the traction and directional cosines:

$$S_{x'z'}^p = S_{z'x'}^p = \vec{T} \cdot \vec{e}_{x'} = A_h \delta p \sin \delta \cos \delta \cos^2 \phi + A_H \delta p \sin \delta \cos \delta \sin^2 \phi \quad , \quad (9.1)$$

$$S_{y'z'}^p = S_{z'y'}^p = \vec{T} \cdot \vec{e}_{y'} = (A_h - A_H) \delta p \sin \delta \sin \phi \cos \phi \quad , \quad (9.2)$$

$$S_{z'z'}^p = \vec{T} \cdot \vec{e}_{z'} = A_h \delta p \sin^2 \delta \cos^2 \phi + A_H \delta p \sin^2 \delta \sin^2 \phi \quad . \quad (9.3)$$

The corresponding maximum shear stress on the fault is thus:

$$\tau_{\max} = \sqrt{(S_{x'z'}^p)^2 + (S_{y'z'}^p)^2} = \sqrt{T_i T_i - (S_{z'z'}^p)^2} \quad , \quad (10)$$

and the stress perturbation tensor in x' - y' - z' is:

$$S_{i'j'}^p = \begin{bmatrix} 0 & 0 & S_{x'z'}^p \\ 0 & 0 & S_{y'z'}^p \\ S_{z'x'}^p & S_{z'y'}^p & S_{z'z'}^p \end{bmatrix} \quad . \quad (11)$$

The stress perturbation tensor in x - y - z can be obtained via the following stress transformation:

$$S_{ij}^p = A^T S_{i'j'}^p A \quad , \quad (12)$$

where

$$A = \begin{pmatrix} \hat{e}_x^T \\ \hat{e}_y^T \\ \hat{e}_z^T \end{pmatrix} \begin{pmatrix} e_x^T \\ e_y^T \\ e_z^T \end{pmatrix} \quad . \quad (13)$$

The new stress state in x-y-z can be found by adding E.q.(3) and E.q.(12):

$$S_{ij}^{new} = S_{ij}^B + S_{ij}^p \quad . \quad (14)$$

The new principal stresses and their orientations can be found by solving for the eigenvalues and eigenvectors of the new stress tensor:

$$\det(S_{ij}^{new} - \lambda \delta_{ij}) = 0 \quad , \quad (15.1)$$

$$(S_{ij}^{new} - \lambda \delta_{ij}) l_j = 0 \quad . \quad (15.2)$$

The absolute net rotation in 3D space is given by:

$$\gamma = \cos^{-1} \left(\frac{\bar{a} \cdot \bar{b}}{|\bar{a}| |\bar{b}|} \right) \quad , \quad (16)$$

where \bar{a} and \bar{b} represent the old and the new principal stress directions. Take the acute angle:

$$\gamma = \begin{cases} \gamma, & \gamma \leq \pi/2 \\ \pi - \gamma, & \pi/2 < \gamma \leq \pi \end{cases} \quad . \quad (17)$$

The new effective stress state within the reservoir is:

$$\sigma_{ij}^{new} = S_{ij}^{new} - a(p + \delta p) \delta_{ij} \quad . \quad (18)$$

Using the effective stress tensor, we can calculate the effective normal stress and shear stress on the fault for determination of the CFF value and stability of the fault.

4. Determine stress path tensor using poroelastic plane strain solutions and frictional equilibrium theory

4.1 Plane strain solution for three principal stresses

Assume a homogeneous, isotropic, and linear-elastic reservoir with a uniform pore pressure distribution. Using Hooke's law:

$$2\mu\varepsilon_{ij} = S_{ij} - \frac{\nu}{1+\nu} S_{kk} \delta_{ij} - \frac{1-2\nu}{1+\nu} \alpha p \delta_{ij} \quad . \quad (19)$$

Assume plane strain along the direction of the intermediate principal stress ($\varepsilon_2=0$), we arrive at the following (note that ε_3 is coupled with pore pressure):

$$S_2 = \nu(S_1 + S_3) + (1-2\nu)\alpha p \quad , \quad (20.1)$$

$$S_3 = \frac{\nu}{1-\nu} S_1 + \frac{1-2\nu}{1-\nu} \alpha p + \frac{2\mu}{1-\nu} \varepsilon_3 \quad , \quad (20.2)$$

$$S_1 = \frac{1-\nu}{\nu} S_3 - \frac{1-2\nu}{\nu} \alpha p - \frac{2\mu}{\nu} \varepsilon_3 \quad . \quad (20.3)$$

4.2 Normal faulting regime

In this case, $S_v=S_1$, $S_{Hmax}=S_2$, $S_{hmin}=S_3$, and $\varepsilon_H=0$. Thus the two horizontal principal stresses are:

$$S_h = \frac{\nu}{1-\nu} S_v + \frac{1-2\nu}{1-\nu} \alpha p + \frac{2\mu}{1-\nu} \varepsilon_h \quad , \quad (21.1)$$

$$S_H = \nu(S_v + S_h) + (1-2\nu)\alpha p \quad , \quad (21.2)$$

and the two corresponding stress paths are:

$$A_h = \frac{\partial S_h}{\partial p} = \alpha \frac{1-2\nu}{1-\nu} + \frac{2\mu}{1-\nu} \frac{\partial \varepsilon_h}{\partial p} \quad , \quad (22.1)$$

$$A_H = \frac{\partial S_H}{\partial p} = \nu A_h + \alpha(1-2\nu) \quad . \quad (22.2)$$

Unfortunately, further information is required in order to determine $\partial \varepsilon_h / \partial p$. Here, we further assume $\varepsilon_h=0$; under this assumption, the case reduces to a **uniaxial strain model** that is suitable for a laterally extensive reservoir with respect to reservoir thickness, and the stress paths reduce to:

$$A_h = A_H = \frac{\partial S_h}{\partial p} = \frac{\partial S_H}{\partial p} = \alpha \frac{1-2\nu}{1-\nu} \quad . \quad (23)$$

In the case where in-situ horizontal principal stresses are anisotropic, we further assume that the initial stress state is one of frictional equilibrium, hence:

$$S_h = \frac{1}{K} S_v + \frac{K-1}{K} \alpha p \quad . \quad (24)$$

Here

$$K = \left(\sqrt{\mu^2 + 1} + \mu \right)^2 \quad , \quad (25)$$

where μ is the coefficient of friction.

We define a stress ratio as:

$$\phi = \frac{S_2 - S_3}{S_1 - S_3} \quad . \quad (26)$$

Thus S_{Hmax} becomes:

$$S_H = \phi S_v + (1 - \phi) S_h \quad . \quad (27)$$

Two stress paths are given by:

$$A_h = c \frac{\partial S_h}{\partial p} = c \frac{K-1}{K} \alpha \quad , \quad (28.1)$$

$$A_H = \frac{\partial S_H}{\partial p} = (1 - \phi) A_h \quad , \quad (28.2)$$

where c is introduced as a perturbation factor, which allows depletion to perturb the initial frictional equilibrium ($c > 1$ for depletion). We call this a **synthetic model**.

4.3 Reverse faulting regime

In this case, $S_{Hmax} = S_1$, $S_{Hmin} = S_2$, $S_v = S_3$, and $\varepsilon_H = 0$. Thus the two horizontal principal stresses are:

$$S_H = \frac{1-\nu}{\nu} S_v - \frac{1-2\nu}{\nu} \alpha p - \frac{2\mu}{\nu} \varepsilon_v \quad , \quad (29.1)$$

$$S_h = \nu(S_H + S_v) + (1-2\nu)\alpha p \quad , \quad (29.2)$$

and the two stress paths are:

$$A_H = \frac{\partial S_H}{\partial p} = -\frac{1-2\nu}{\nu} \alpha - \frac{2\mu}{\nu} \frac{\partial \varepsilon_v}{\partial p} \quad , \quad (30.1)$$

$$A_h = \frac{\partial S_h}{\partial p} = \nu A_H + \alpha(1-2\nu) \quad . \quad (30.2)$$

Similarly, if we further assume $\varepsilon_v = 0$, the stress paths reduce to:

$$A_H = \frac{\partial S_H}{\partial p} = -\alpha \frac{1-2\nu}{\nu} \quad , \quad (31.1)$$

$$A_h = 0 \quad , \quad (31.2)$$

This is suitable for a reservoir with a significantly stiff caprock that inhibits vertical strain. We refer this as a **stiff caprock model** in this study.

4.4 Strike-slip faulting regime

In this case, $S_{Hmax}=S_1$, $S_v=S_2$, $S_{hmin}=S_3$, and $\varepsilon_v=0$. Eq.(20.1) becomes:

$$S_v = \nu(S_H + S_h) + (1-2\nu)\alpha p \quad , \quad (32)$$

Taking derivatives with respect to p gives a relation between A_h and A_H :

$$A_H + A_h = \frac{\partial S_H}{\partial p} + \frac{\partial S_h}{\partial p} = -\alpha \frac{1-2\nu}{\nu} \quad . \quad (33)$$

Again, if we further assume that the initial stress state is one of frictional equilibrium, we get:

$$S_H = KS_h + (1-K)\alpha p \quad . \quad (34)$$

Substituting Eq.(34) into E.q.(32) and rearranging gives:

$$S_h = \frac{1}{\nu(1+K)} S_v - \frac{1-\nu(1+K)}{\nu(1+K)} \alpha p \quad . \quad (35)$$

The stress paths are thus:

$$A_h = \frac{\partial S_h}{\partial p} = -\frac{1-\nu(1+K)}{\nu(1+K)} \alpha \quad , \quad (36)$$

$$A_H = -\alpha \frac{1-2\nu}{\nu} - A_h \quad (37)$$

In the following hypothetical studies, this will be referred to as a **hybrid model**.

5. Hypothetical case studies

Here, the changes in magnitude and the net 3D rotations of the three principal stresses and the resulting changes in the Coulomb Failure Function will be demonstrated via hypothetical case studies under three faulting regimes. A polar coordinate system, as explained below, is introduced for visualization purposes.

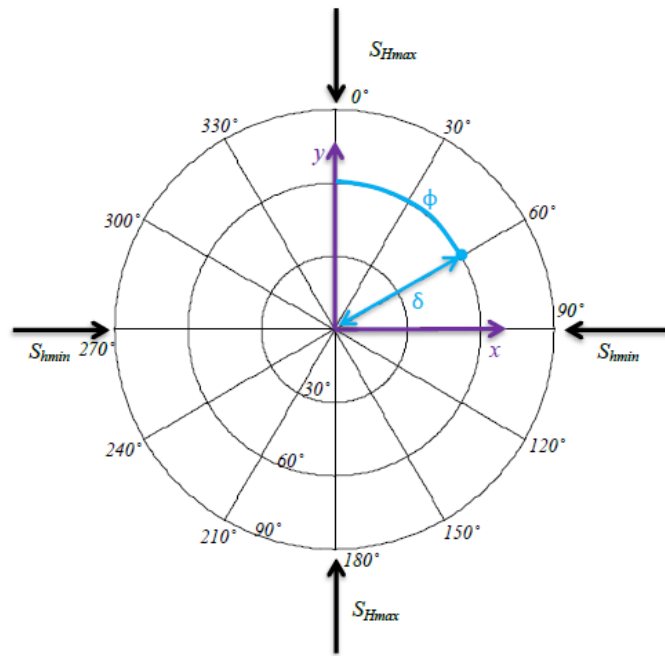


Figure2: Polar coordinates introduced for visualization in this study. Location of the blue dot represents the fault orientation with respect to the stress field: ϕ is the fault azimuth with respect to y direction (one of the S_{Hmax} directions), and δ is the fault dip. In this case, it represents a fault of azimuth 60° relative to y direction and dipping at 60° . Note that S_{Hmax} is not necessarily along a north-south axis.

5.1 Normal faulting regime: uniaxial strain model

For demonstration purposes, consider the following hypothetical variable values: depth=2000m, overburden density $\rho_{average}=2300\text{kgm}^{-3}$, P_p = hydrostatic $\times 120\%$. S_{Hmax} and S_{Hmin} are calculated using Eq.(21.1), Eq.(21.2) by setting lateral strain to 0. These give an initial stress state $S_V=46\text{MPa}$, $S_{Hmax}=S_{Hmin}=28.13\text{MPa}$, and $P_p=24\text{MPa}$. Other parameters: $\alpha=0.8$, $\nu=0.25$, $\mu=0.6$. These yield stress path $A_h=A_H=0.53$ using Eq.(23).

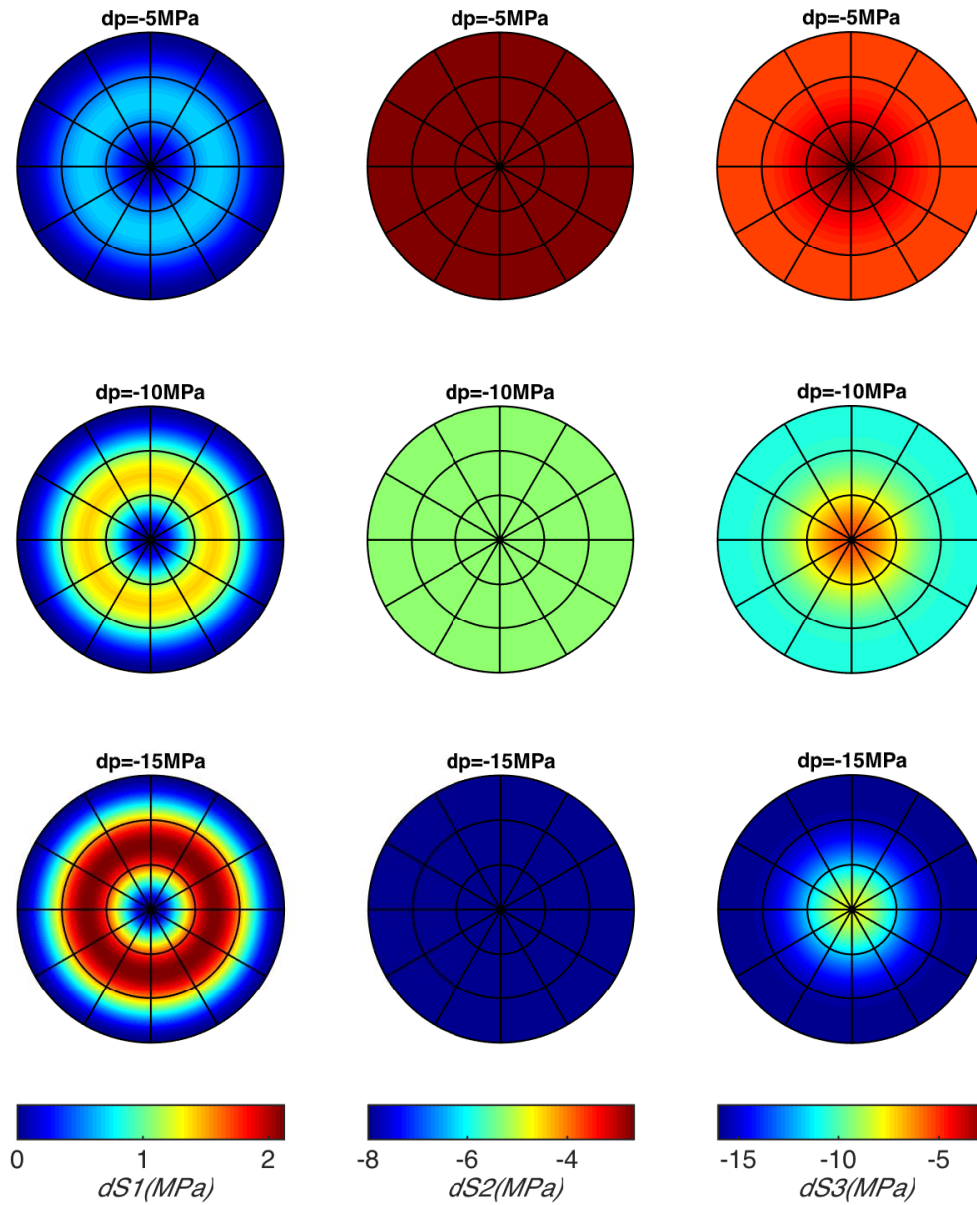


Figure 3: Changes of the magnitude of principal stress S_1 (left), S_2 (middle) and S_3 (right), for depletion of -5 MPa (upper), -10 MPa (middle) and -15 MPa (lower). Three columns are assigned their respective color scales. Within each column, the three rows share the same color scale.

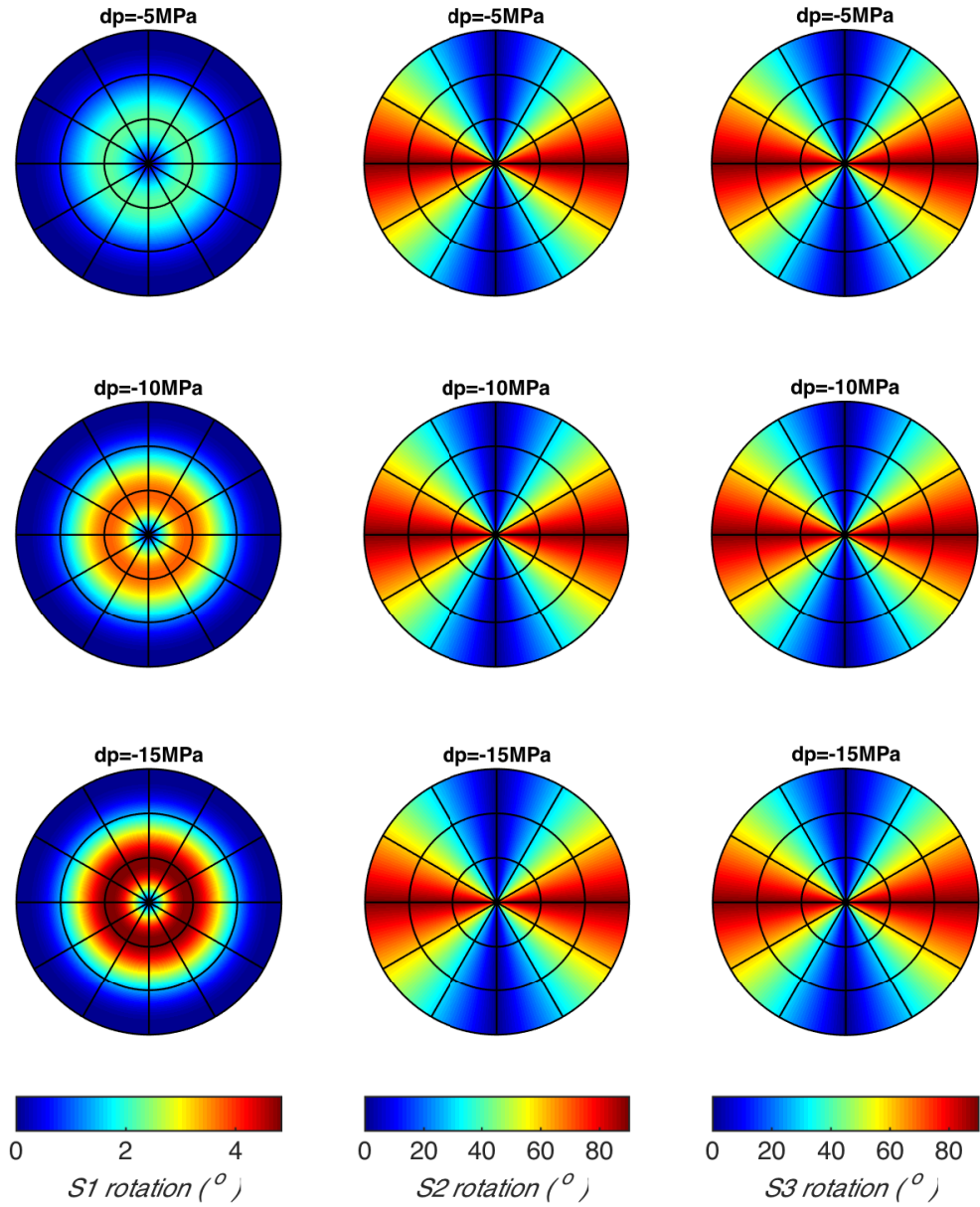


Figure 4: 3D net rotations of principal stress $S1$ (left), $S2$ (middle) and $S3$ (right), for depletion of -5 MPa (upper), -10 MPa (middle) and -15 MPa (lower). Three columns are assigned their respective color scales. Within each column, the three rows share the same color scale.

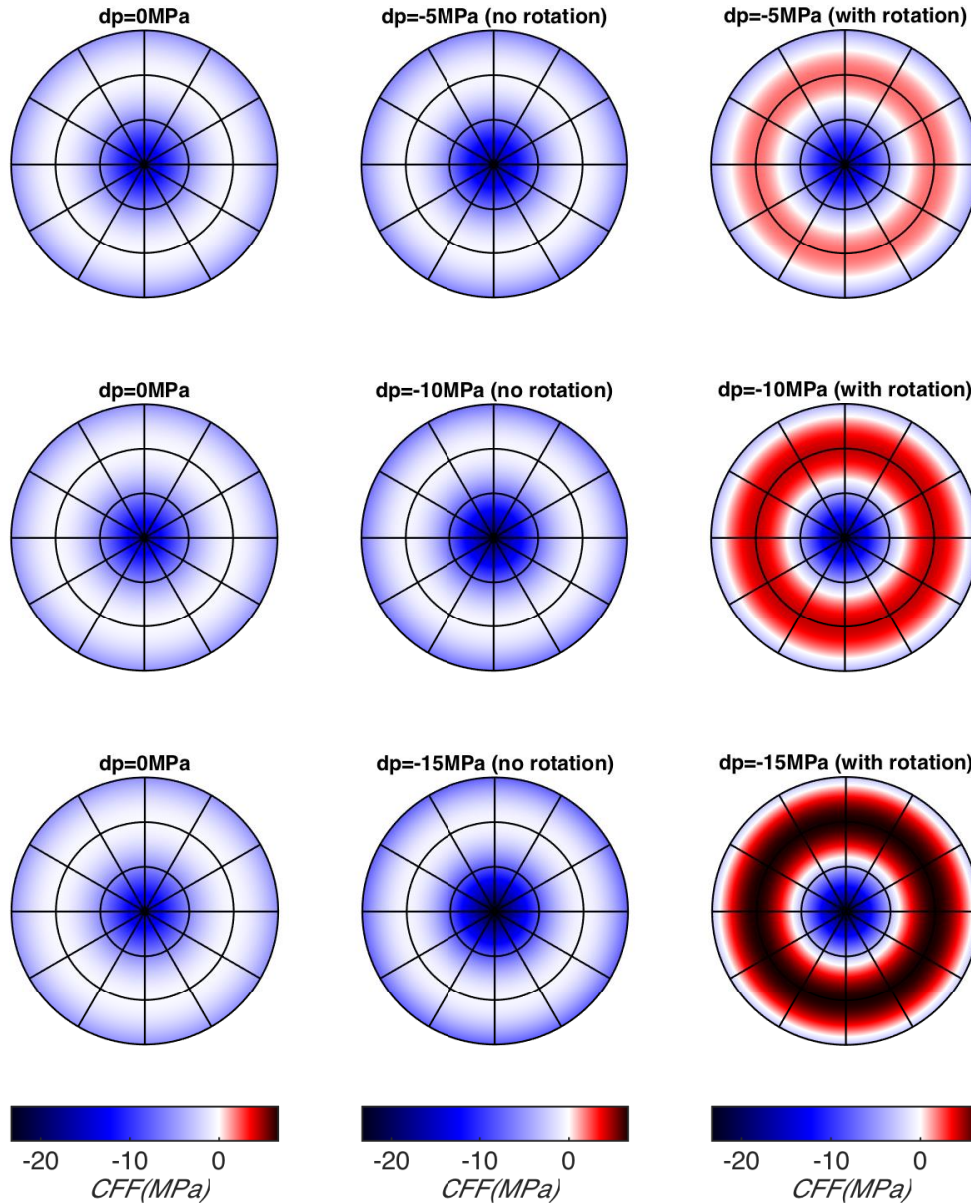


Figure 5: Changes of the Coulomb Failure Functions. Left: Before depletion; middle: after depletion without rotation (depletion occurs on both sides of the fault); right: after depletion with rotation (depletion occurs on one side of the fault). Pore pressure depletions are -5MPa (upper), -10MPa (middle) and -15 MPa (lower). Blue indicates the orientation of a stable fault, while red indicates the orientation of a fault that will be induced to slip due to depletion. All plots share the same color scale. Comparison of the left and middle images clearly shows that depletion induces slip on faults of certain orientations due to the poroelastic coupling effect; comparison of the middle and right images shows that stress rotation induces faults that are even less favorably oriented to slip.

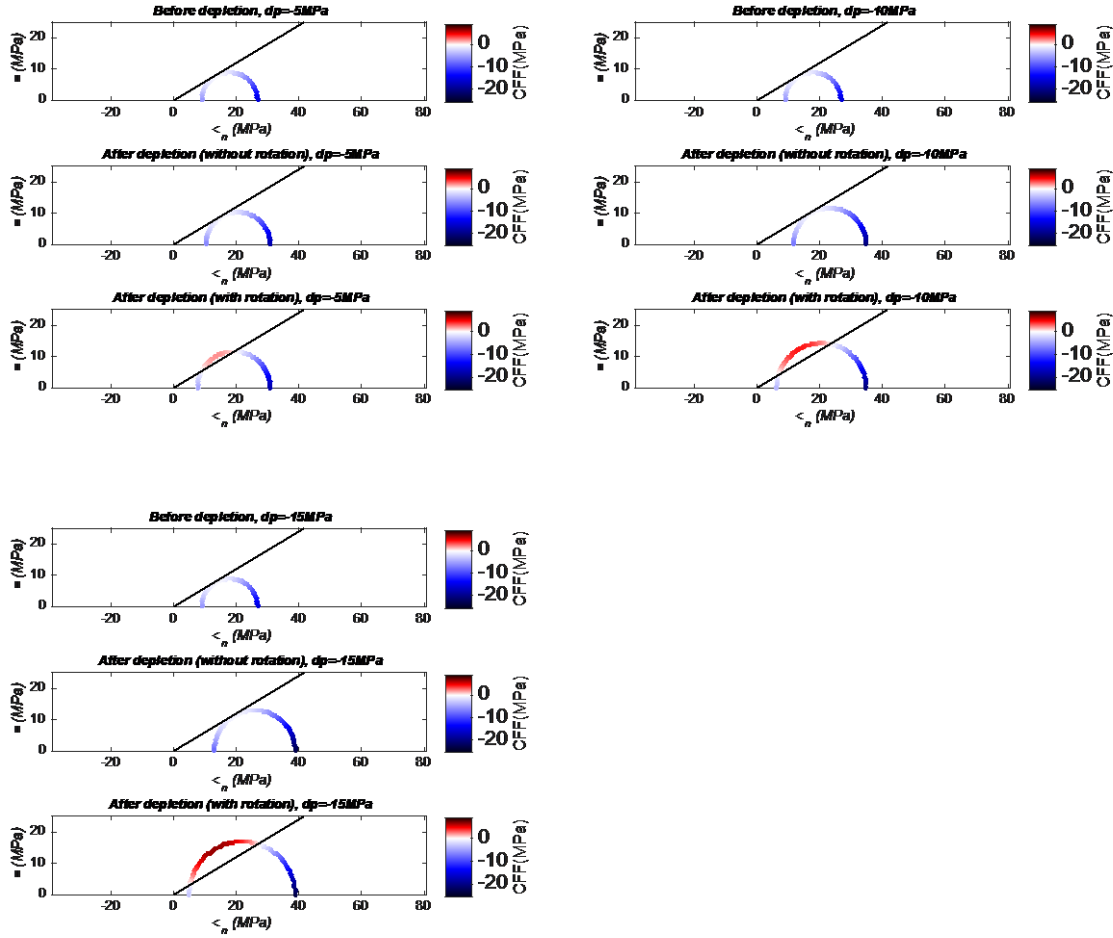


Figure 6: Mohr circles. Fault orientations are mapped into τ - σ_n space and colored by CFF values. Pore pressure depletions are 5MPa (upper left), -10MPa (upper right) and -15 MPa (lower). In each case, upper: before depletion; middle: after depletion, without rotation (depletion occurs on both sides of the fault); lower: after depletion, with rotation (depletion occurs on one side of the fault). This plot shows in a different way how depletion induces slip on certain faults, and how stress rotation brings more faults towards shear failure.

5.2 Normal faulting regime: synthetic model

Consider the following hypothetical case: depth=2000m, overburden density $\rho_{\text{average}} = 2300\text{kgm}^{-3}$, $P_p = \text{hydrostatic} \times 120\%$. $S_{H_{\text{max}}}$ and $S_{H_{\text{min}}}$ are calculated using Eq.(24), Eq(27). These give an initial stress state with $S_v = 46\text{MPa}$, $S_{H_{\text{max}}} = 36.89\text{MPa}$, $S_{H_{\text{min}}} = 27.79\text{MPa}$, and $P_p = 24\text{MPa}$. Other parameters: $\alpha = 0.8$, $\gamma = 0.25$, $\mu = 0.6$, $\phi = 0.5$, $c = 1.25$. These yield stress path $A_H = 0.34$, $A_h = 0.68$ using Eq.(28.1), Eq(28.2).

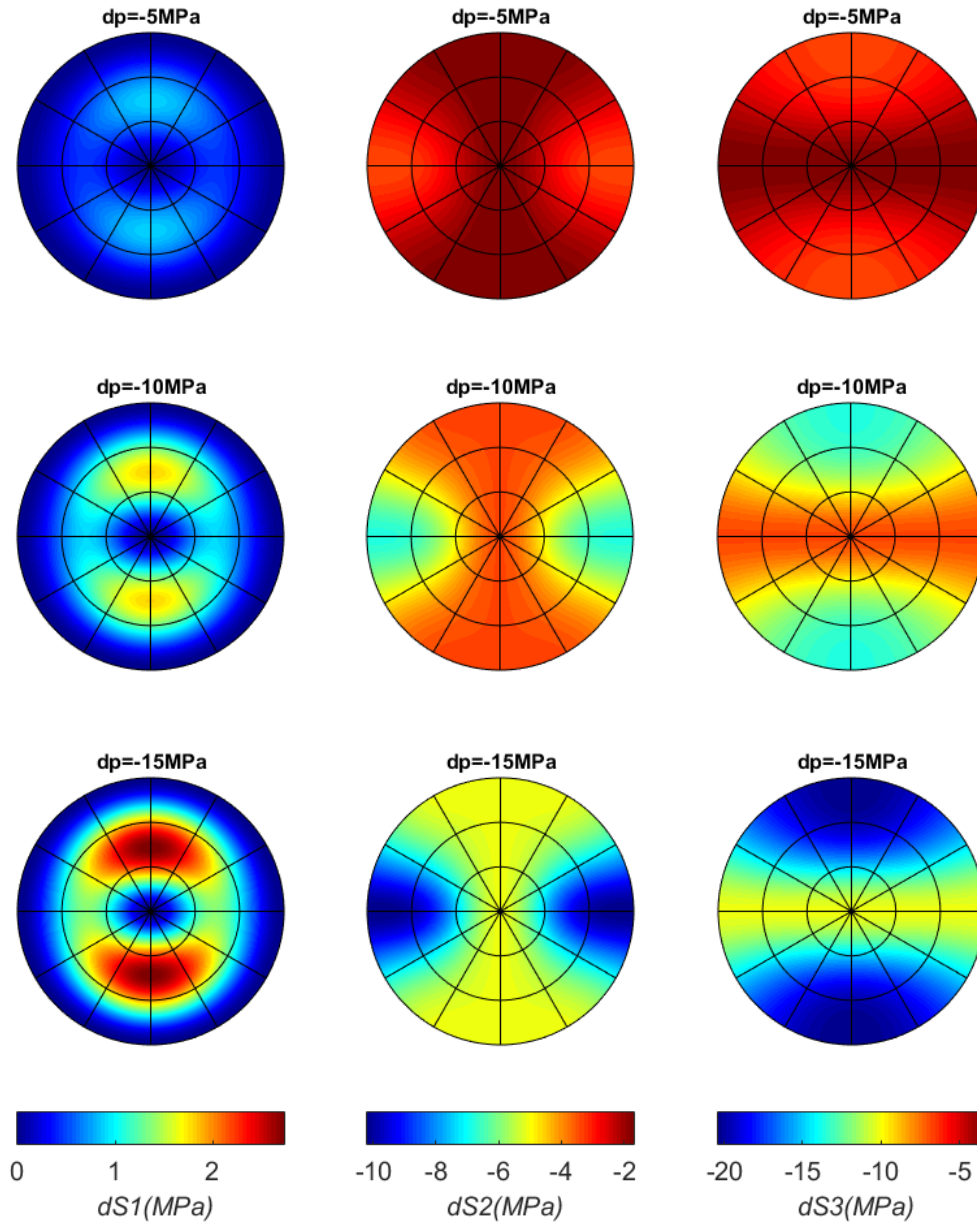


Figure 7: Changes of magnitude of principal stress S_1 (left), S_2 (middle) and S_3 (right), for pore pressure depletion of -5MPa (upper), -10MPa (middle) and -15MPa (lower). Three columns are assigned their respective color scales. Within each column, the three rows share the same color scale.

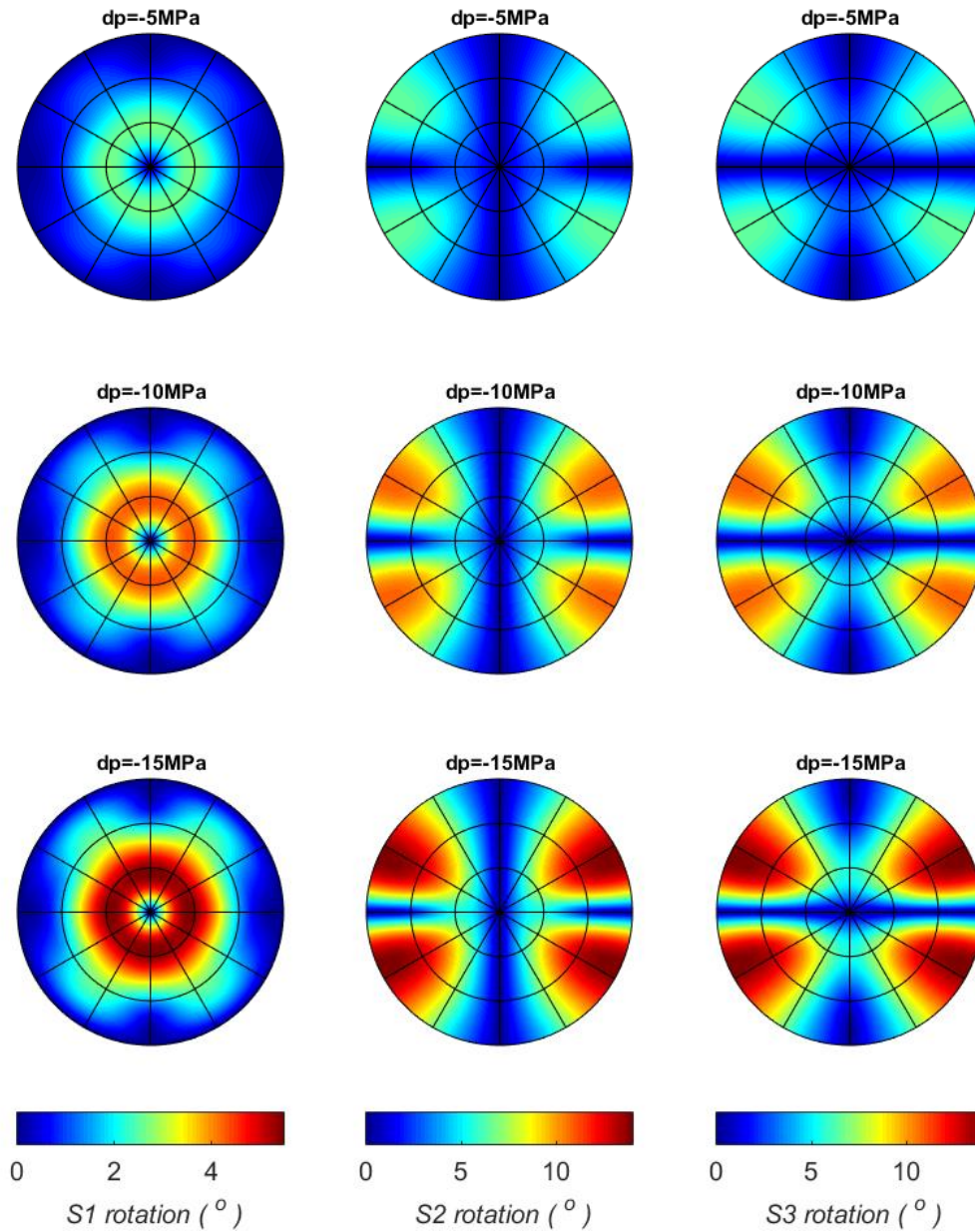


Figure 8: 3D net rotations of principal stress S_1 (left), S_2 (middle) and S_3 (right), for pore pressure depletion of -5MPa (upper), -10MPa (middle) and -15MPa (lower). A same color scale is assigned to each principal stress undergoing three different pore pressure changes.

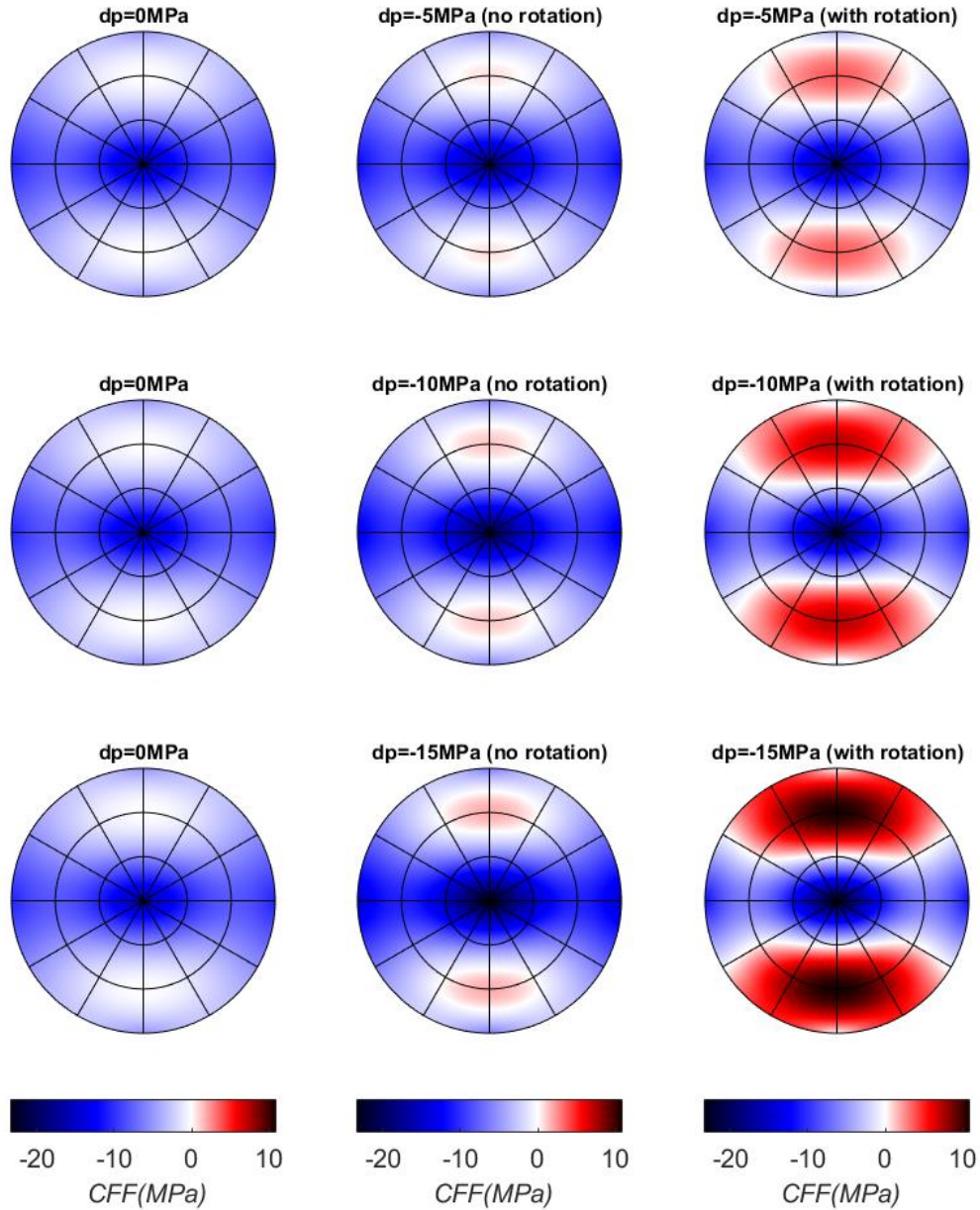


Figure 9: CFF values for the same hypothetical case study. Left: Before depletion; middle: after depletion, without rotation (depletion occurs on both sides of the fault); right: after depletion, with rotation (depletion occurs on one side of the fault). Pore pressure depletions are -5MPa (upper), -10MPa (middle) and -15 MPa (lower). Blue indicates the orientation of a stable fault, while red indicates the orientation of a fault that will be induced to slip due to depletion. Again, comparison of the left and middle images clearly shows that depletion induces slip on faults of certain orientations due to the poroelastic coupling effect; comparison of the middle and right images shows that stress rotation induces faults that are even less favorably oriented to slip.

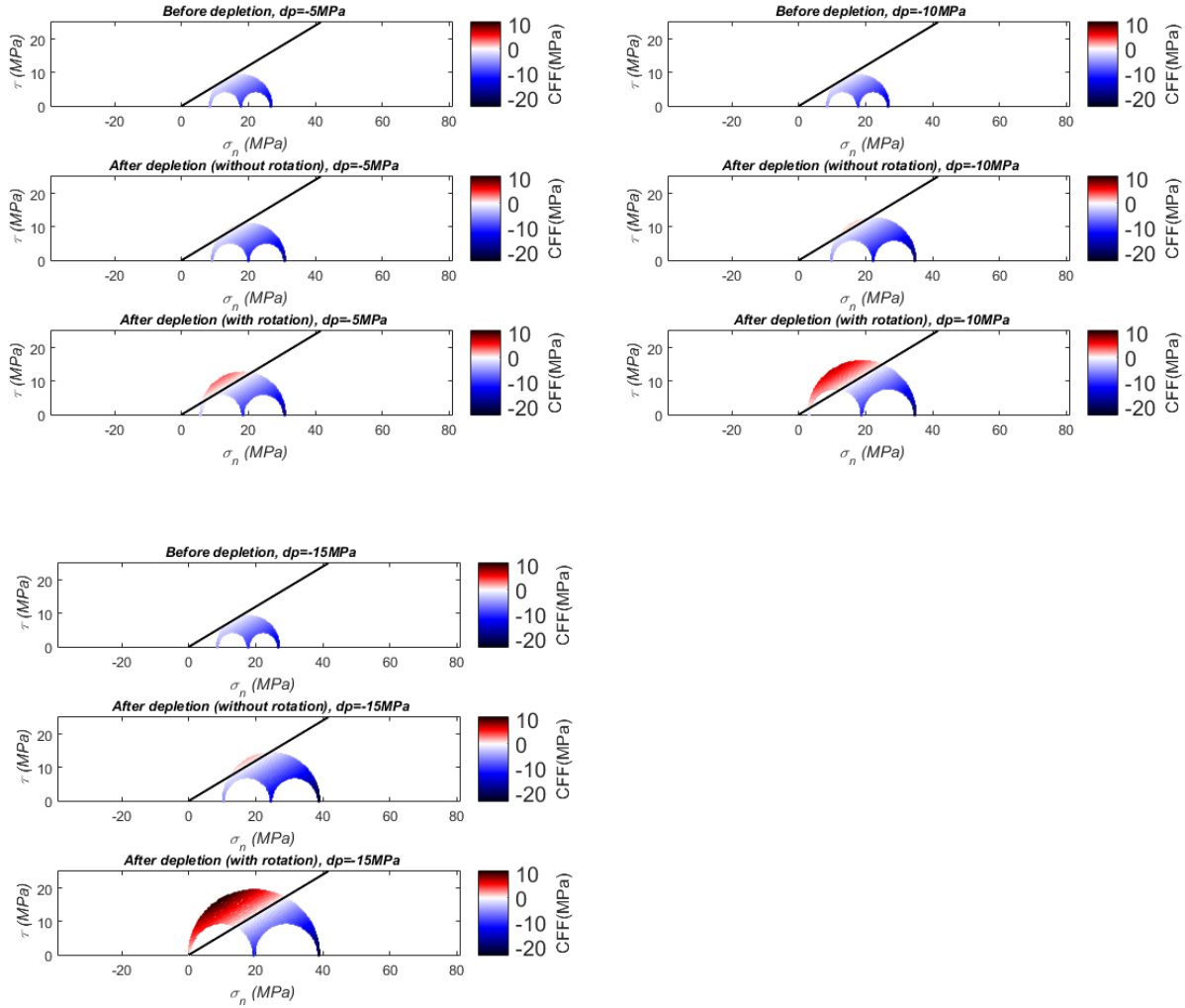


Figure 10: Mohr circles. Fault orientations are mapped into τ - σ_n space and colored by CFF values. Pore pressure depletions are 5MPa (upper left), -10MPa (upper right) and -15 MPa (lower). In each case, upper: before depletion; middle: after depletion, without rotation (depletion occurs on both sides of the fault); lower: after depletion, with rotation (depletion occurs on one side of the fault). Again this plot shows in a different way how depletion induces slip on certain faults, and how stress rotation brings more faults towards shear failure.

5.3 Reverse faulting regime: stiff caprock model

Consider the following hypothetical case: depth=2000m, overburden density $\rho_{\text{average}}=2300\text{kgm}^{-3}$, P_p = hydrostatic $\times 120\%$. $S_{H\text{max}}$ and $S_{H\text{min}}$ are calculated using Eq.(29.1), Eq.(29.2). These give an initial stress state with $S_v=46\text{MPa}$, $S_{H\text{max}}=99.6\text{MPa}$, $S_{H\text{min}}=46\text{MPa}$, and $P_p=24\text{MPa}$. For calculation purposes, a 2MPa perturbation was added to $S_{H\text{min}}$. Other parameters: $\alpha=0.8$, $\gamma=0.25$, $\mu=0.6$. These yield stress path $A_H=-1.60$, $A_h= 0$ using Eq.(30.1), Eq.(30.2).

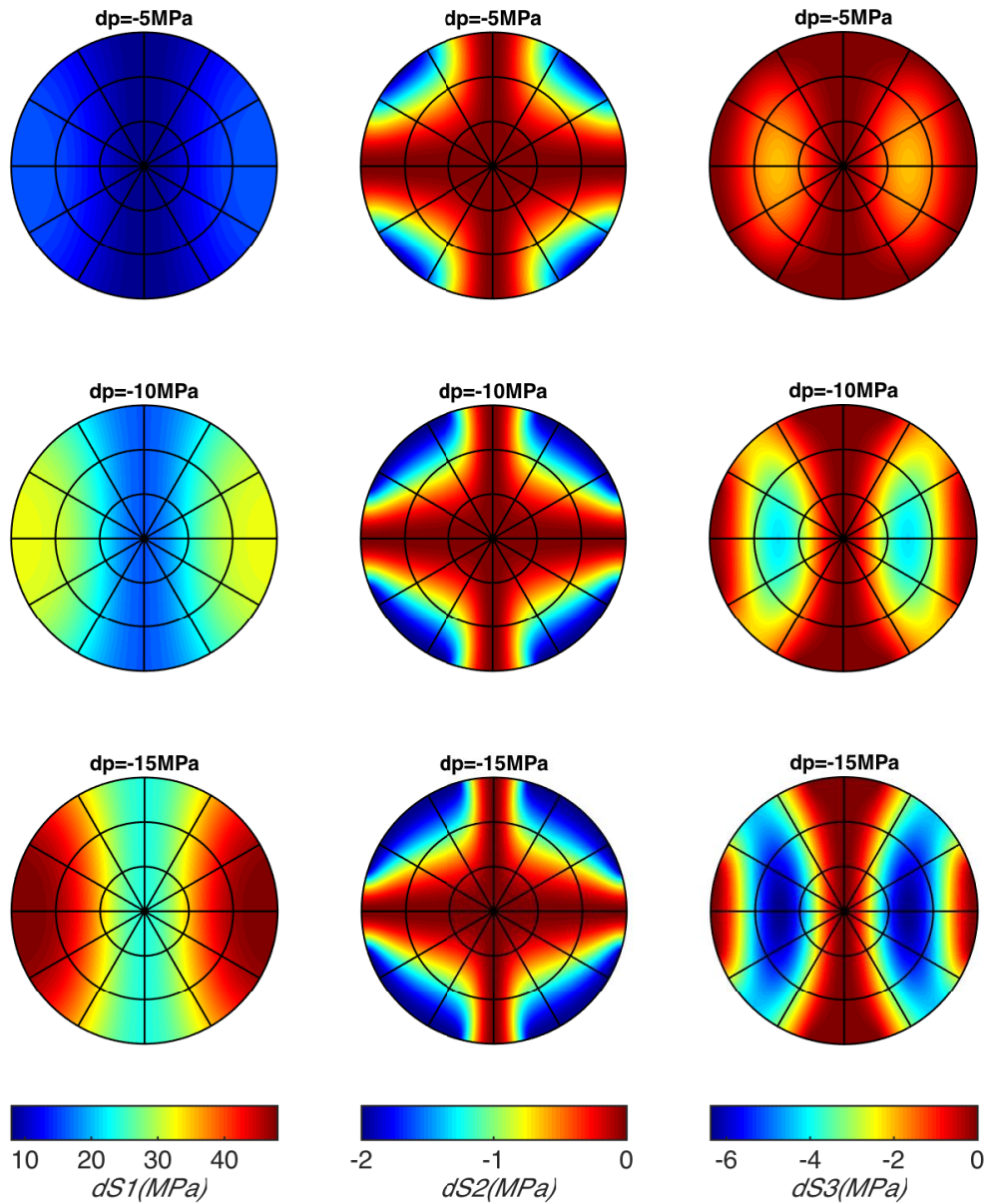


Figure 11: Changes of magnitude of principal stress S_1 (left), S_2 (middle) and S_3 (right), for pore pressure depletion of -5MPa (upper), -10MPa (middle) and -15MPa (lower). Three columns are assigned their respective color scales. Within each column, the three rows share the same color scale.

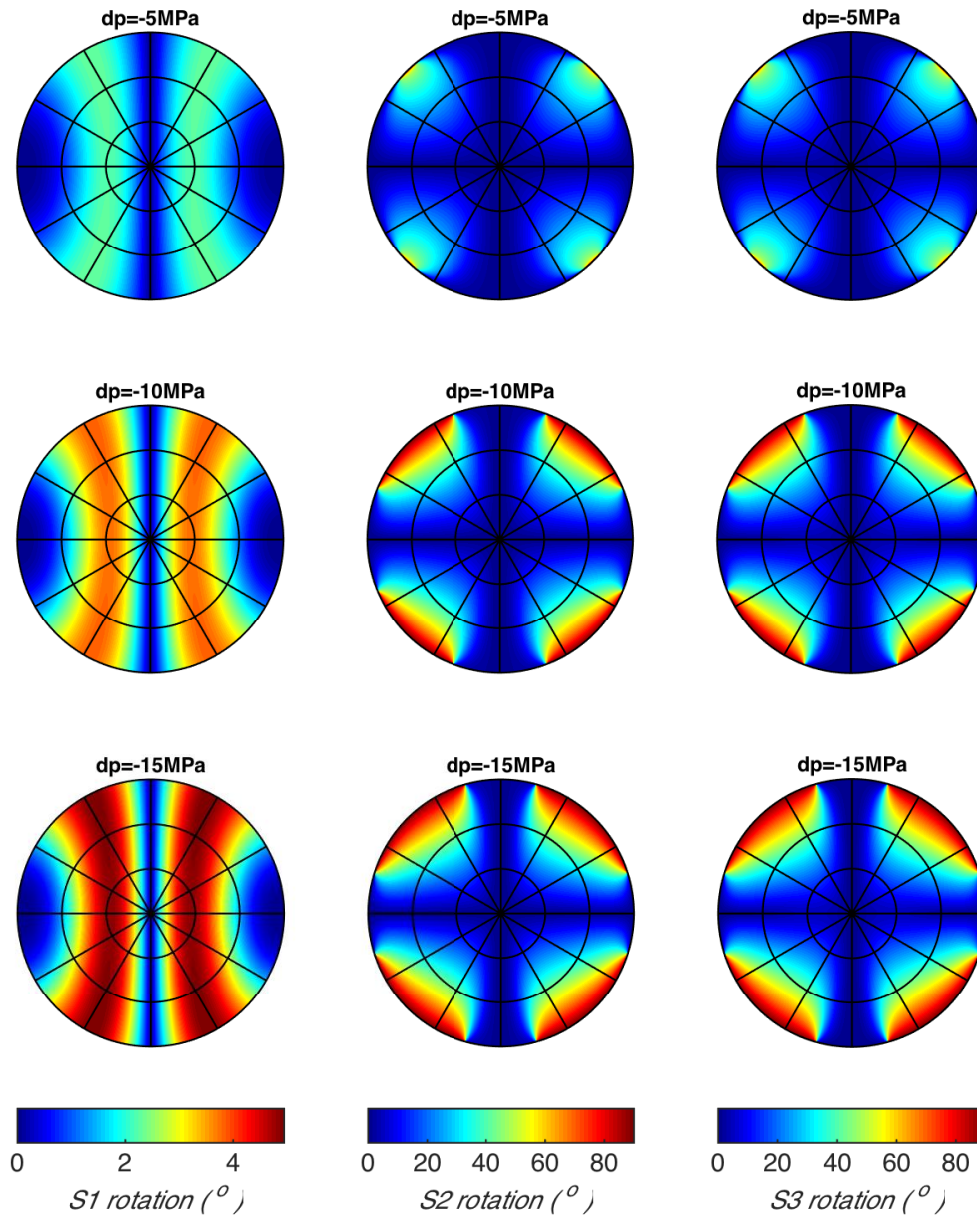


Figure 12: 3D net rotations of principal stress S_1 (left), S_2 (middle) and S_3 (right), for pore pressure depletion of -5MPa (upper), -10MPa (middle) and -15MPa (lower). A same color scale is assigned to each principal stress undergoing three different pore pressure changes.

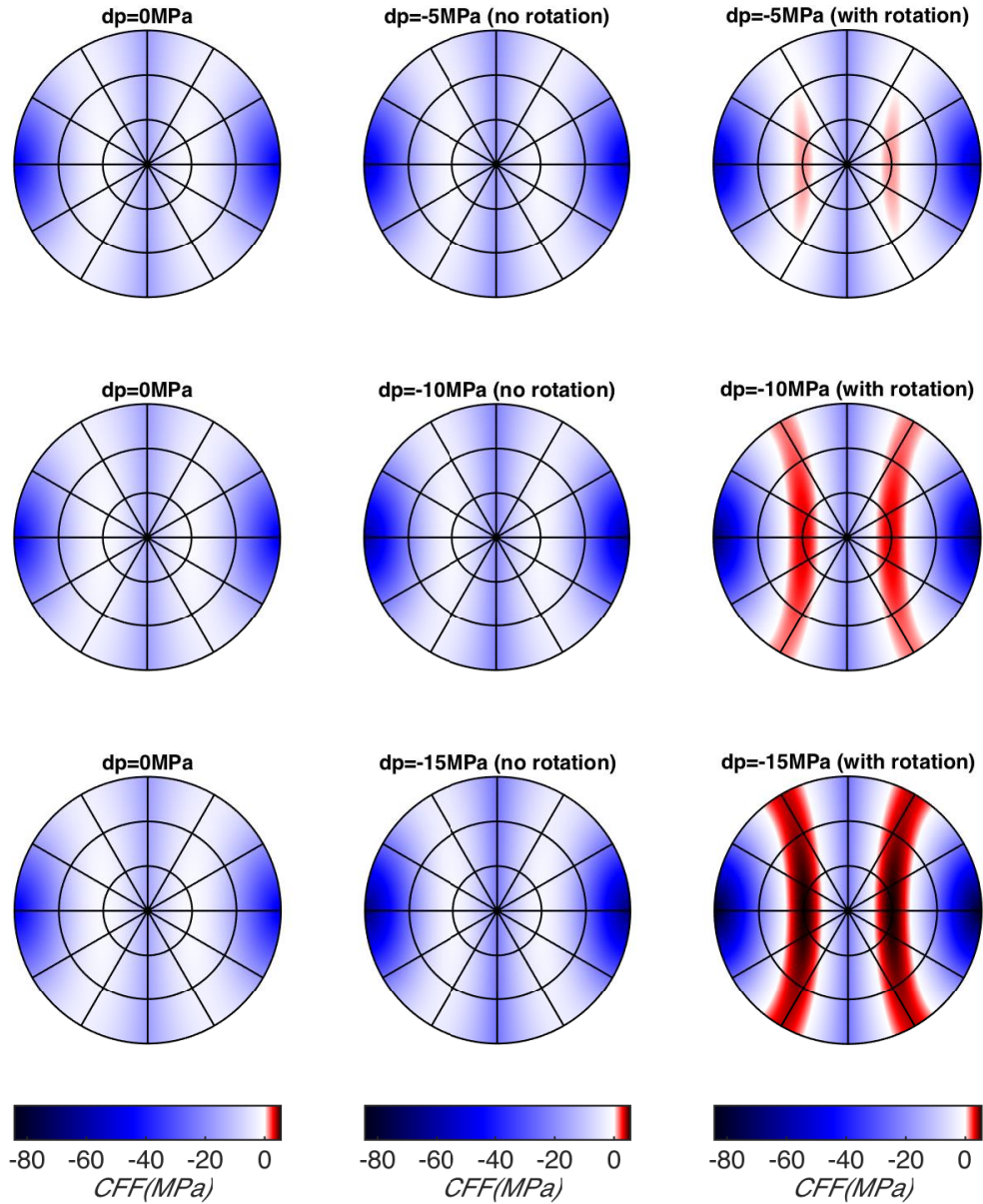


Figure 13: Mohr circles. Fault orientations are mapped into τ - σ_n space and colored by CFF values. Pore pressure depletions are 5MPa (upper left), -10MPa (upper right) and -15 MPa (lower). In each case, upper: before depletion; middle: after depletion, without rotation (depletion occurs on both sides of the fault); lower: after depletion, with rotation (depletion occurs on one side of the fault). Again this plot shows in a different way how depletion induces slip on certain faults, and how stress rotation brings more faults towards shear failure.

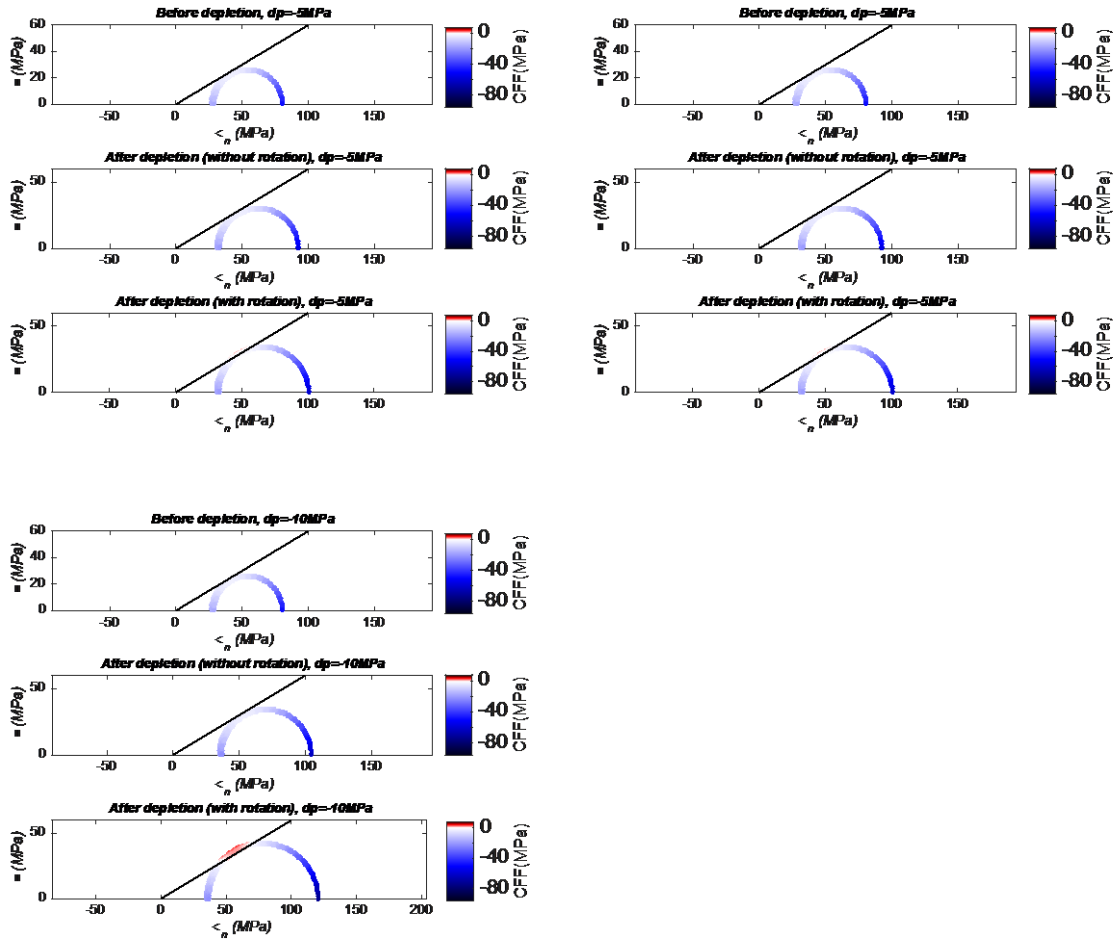


Figure 14: Mohr circles. Fault orientations are mapped into τ - σ_n space and colored by CFF values. Pore pressure depletions are 5MPa (upper left), -10MPa (upper right) and -15 MPa (lower). In each case, upper: before depletion; middle: after depletion, without rotation (depletion occurs on both sides of the fault); lower: after depletion, with rotation (depletion occurs on one side of the fault). Again this plot shows in a different way how depletion induces slip on certain faults, and how stress rotation brings more faults towards shear failure.

5.4 Strike-slip faulting regime: hybrid model

We design the following hypothetical case: depth=2000m, overburden density $\rho_{\text{average}}=2300\text{kgm}^{-3}$, $P_p=$ hydrostatic $\times 120\%$. $S_{H\text{max}}$ and $S_{h\text{min}}$ are calculated using Eq.(34), Eq.(35). These give an initial stress state with $S_v=46\text{MPa}$, $S_{H\text{max}}=100.38\text{MPa}$, $S_{h\text{min}}=45.22\text{MPa}$, and $P_p=24\text{MPa}$. Other parameters: $\alpha=1.0$, $\gamma=0.25$, $\mu=0.7$. These yield stress path $A_H=-2.1469$, $A_h=0.1469$ using Eq.(36), Eq.(37).

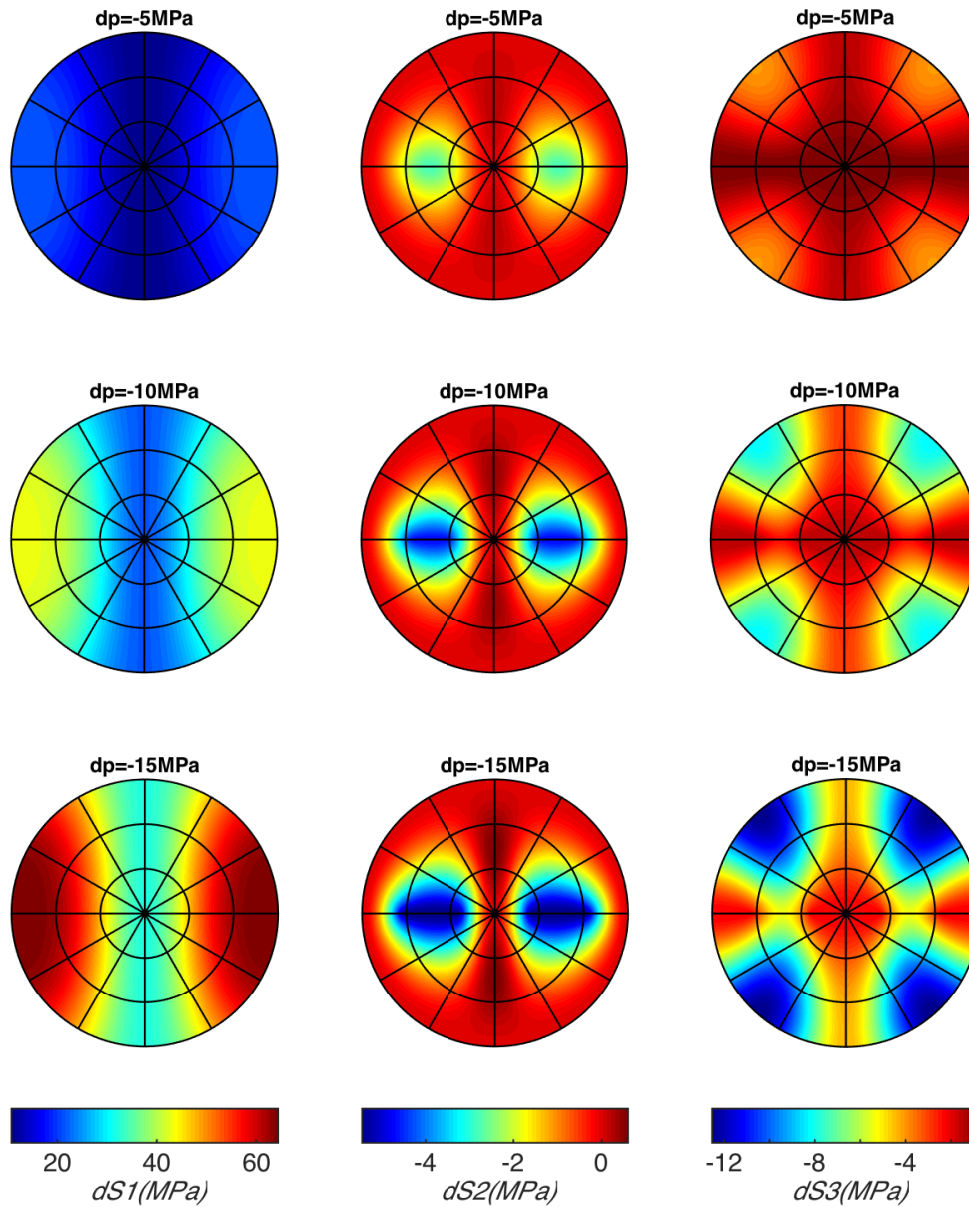


Figure 15: Changes of magnitude of principal stress S_1 (left), S_2 (middle) and S_3 (right), for pore pressure depletion of -5MPa (upper), -10MPa (middle) and -15MPa (lower). Three columns are assigned their respective color scales. Within each column, the three rows share the same color scale.

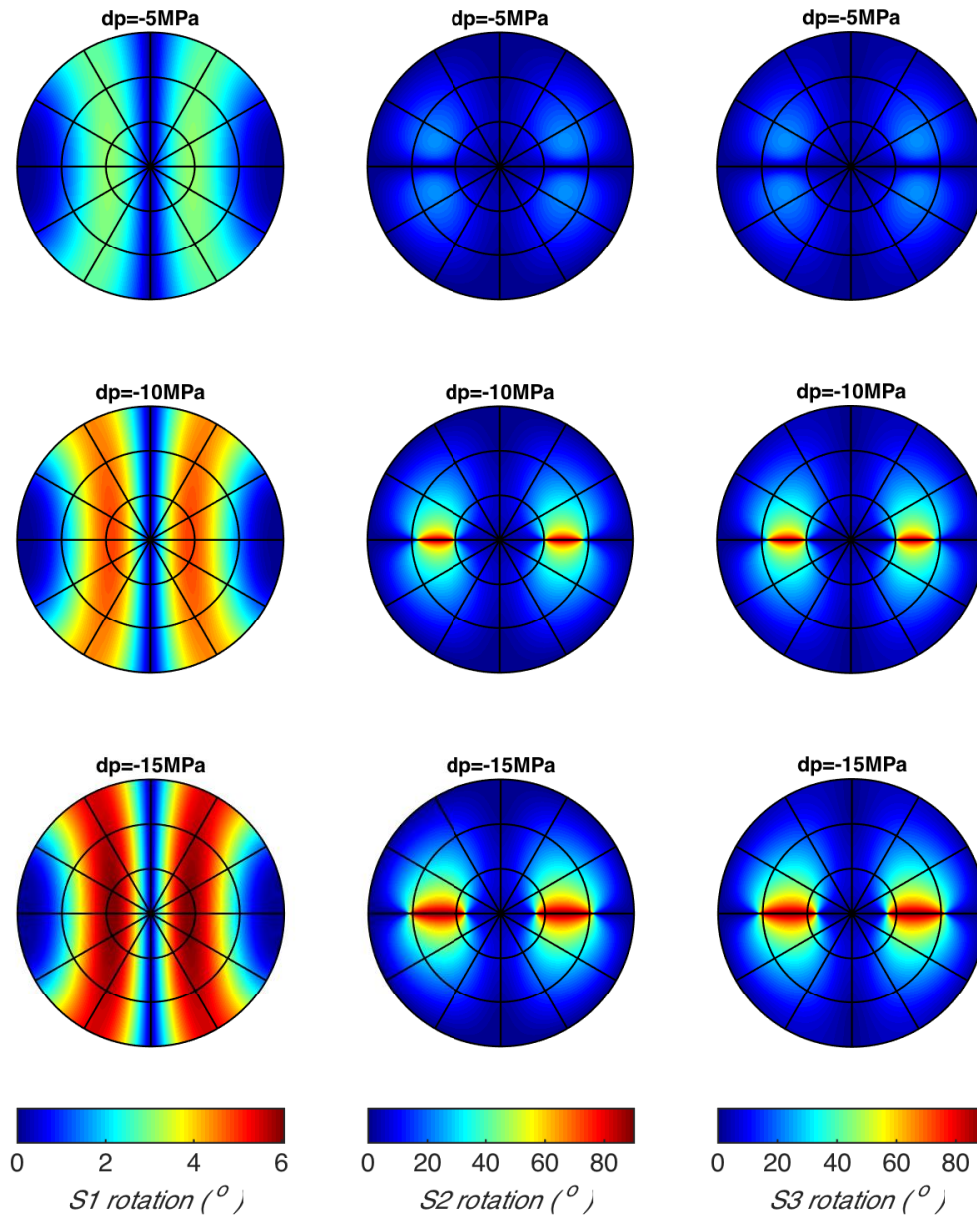


Figure 16: 3D net rotations of principal stress S_1 (left), S_2 (middle) and S_3 (right), for pore pressure depletion of -5MPa (upper), -10MPa (middle) and -15MPa (lower). A same color scale is assigned to each principal stress undergoing three different pore pressure changes.

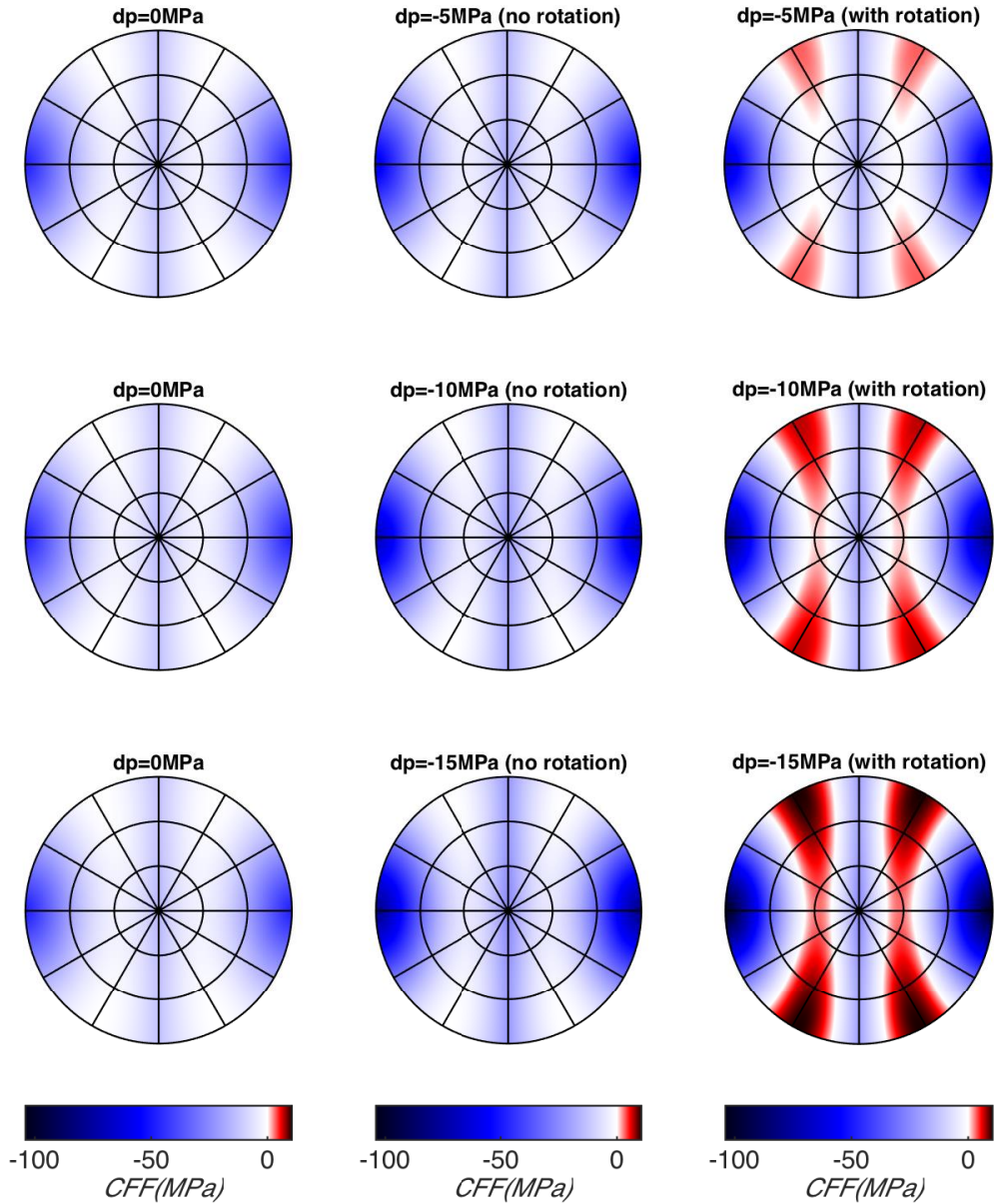


Figure 17: Mohr circles. Fault orientations are mapped into τ - σ_n space and colored by CFF values. Pore pressure depletions are 5MPa (upper left), -10MPa (upper right) and -15 MPa (lower). In each case, upper: before depletion; middle: after depletion, without rotation (depletion occurs on both sides of the fault); lower: after depletion, with rotation (depletion occurs on one side of the fault). Again this plot shows in a different way how depletion induces slip on certain faults, and how stress rotation brings more faults towards shear failure.

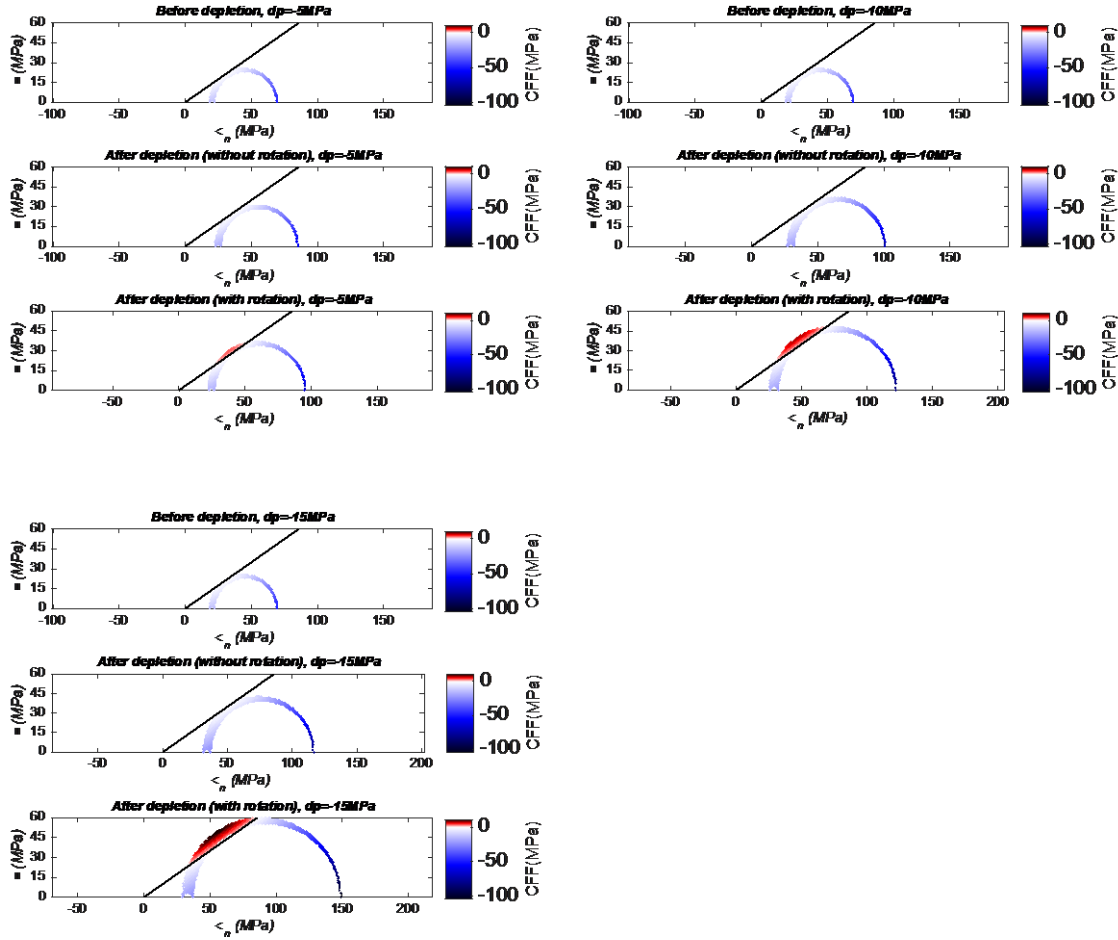


Figure 14: Mohr circles. Fault orientations are mapped into τ - σ_n space and colored by CFF values. Pore pressure depletions are 5MPa (upper left), -10MPa (upper right) and -15 MPa (lower). In each case, upper: before depletion; middle: after depletion, without rotation (depletion occurs on both sides of the fault); lower: after depletion, with rotation (depletion occurs on one side of the fault). Again this plot shows in a different way how depletion induces slip on certain faults, and how stress rotation brings more faults towards shear failure.

6. Conclusion

We propose an additional mechanism for depletion-induced faulting in cases where a reservoir undergoing pore pressure depletion is bounded by a hydraulically impermeable fault. Unbalanced pore pressure changes on the two sides of the fault, in conjunction with complex proelastic responses, cause redistribution of the stresses within the reservoir. When the fault is not in alignment with one of the principal stresses, principal stresses will be re-oriented. Given a fault that is arbitrarily oriented with respect to the original stress field, we derive a generalized 3D analytical solution for the new state of stress after depletion by considering anisotropic stress path. Using this solution, we quantify the changes in magnitude and the rotations of the three principal stresses. We then compare the Coulomb Failure Functions and corresponding Mohr circles for three different cases: before depletion, after depletion without

stress rotation, and after depletion with stress rotation. For demonstration purposes, we determined the stress path tensor using poroelastic plane strain solutions in conjunction with the frictional equilibrium theory for three faulting regimes. Our hypothetical case studies show that, for a bound reservoir, depletion-induced principal stress rotations and magnitude changes have a significant impact on fault stability, and are a complex function of the fault orientation, the original in-situ stress state and pore pressure, the degree of depletion, and the degree of poroelastic coupling.

Acknowledgements

We thank the Stanford Rock Physics and Borehole Geophysics Consortium for financial support.

References

- Aadnoy, B.S., 1991. Effects of reservoir depletion on borehole stability. *Journal of Petroleum Science and Engineering*, 6(1), pp.57–61.
- Addis, M.A., 1997. Reservoir depletion and its effect on wellbore stability evaluation. *International Journal of Rock Mechanics and Mining Sciences*, 34(3), pp.4–e1.
- Altmann, J.B. et al., 2010. Poroelastic contribution to the reservoir stress path. *International Journal of Rock Mechanics and Mining Sciences*, 47(7), pp.1104–1113.
- Day-Lewis, A.D.F. & Zoback, M.D., 2007. Depletion-induced Stress Orientation Changes in Bounded Reservoirs. In *2007 AAPG Annual Convention and Exhibition*.
- Engelder, T., & Fischer, M. P. (1994). Influence of poroelastic behavior on the magnitude of minimum horizontal stress, S_h in overpressured parts of sedimentary basins. *Geology*, 22(10), 949-952.
- Martínez-Garzón, P. et al., 2013. Stress tensor changes related to fluid injection at The Geysers geothermal field, California. *Geophysical Research Letters*, 40(11), pp.2596–2601.
- Eshelby, J.D., 1957. The determination of the elastic field of an ellipsoidal inclusion, and related problems. *Proceedings of the Royal Society of London. Series A. Mathematical and Physical Sciences*, 241(1226), pp.376–396.
- Mourgues, R. & Cobbold, P., 2003. Some tectonic consequences of fluid overpressures and seepage forces as demonstrated by sandbox modelling. *Tectonophysics*, 376(1-2), pp.75–97.
- Hillis, R., 2000. Pore pressure/stress coupling and its implications for seismicity. *Exploration Geophysics*, 31(2), p.448.
- Hillis, R. R. (2001). Coupled changes in pore pressure and stress in oil fields and sedimentary basins. *Petroleum Geoscience*, 7(4), 419-425.
- Rudnicki, J.W., 1999. Alteration of regional stress by reservoirs and other inhomogeneities: stabilizing or destabilizing? In *9th ISRM Congress*. International Society for Rock Mechanics.

Segall, P. & Fitzgerald, S.D., 1998. A note on induced stress changes in hydrocarbon and geothermal reservoirs. *Tectonophysics*, 289(1-3), pp.117-128. Segura, J.M. et al., 2011. Reservoir stress path characterization and its implications for fluid-flow production simulations. *Petroleum Geoscience*, 17(4), pp.335-344.

Schoenball, M. et al., 2014. Change of stress regime during geothermal reservoir stimulation. *Geophysical Research Letters*, 41(4), pp.1163-1170.

Sonder, L.J., 1990. Effects of density contrasts on the orientation of stresses in the lithosphere: Relation to principal stress directions in the Transverse Ranges, California. *Tectonics*, 9(4), pp.761-771.

Tingay, M.R.P. et al., 2003. Pore pressure/stress coupling in Brunei Darussalam -- implications for shale injection. *Geological Society, London, Special Publications*, 216(1), pp.369-379.

Van Ruth, P. et al., 2003. The origin of overpressure in "old" sedimentary basins: an example from the Cooper Basin, Australia. *Geofluids*, 3(2), pp.125-131.

Vidal-Gilbert, S., Nauroy, J.-F. & Brosse, E., 2009. 3D geomechanical modelling for CO₂ geologic storage in the Dogger carbonates of the Paris Basin. *International Journal of Greenhouse Gas Control*, 3(3), pp.288-299.

Zoback, M.D. & Zinke, J.C., 2002. Production-induced normal faulting in the Valhall and Ekofisk oil fields. In *The Mechanism of Induced Seismicity*. Springer, pp. 403-420.

Zoback, M.D., 2010. *Reservoir geomechanics*, Cambridge University Press.

Appendix

A.1 A simplified 2D approach

The simplified 2D analytical solution for quantifying the rotations of the principal stresses is provided by Day-Lewis & Zoback (2007). The stress path is assumed to be the same for both horizontal principal stresses, inducing only a fault-normal stress and no shear stresses.

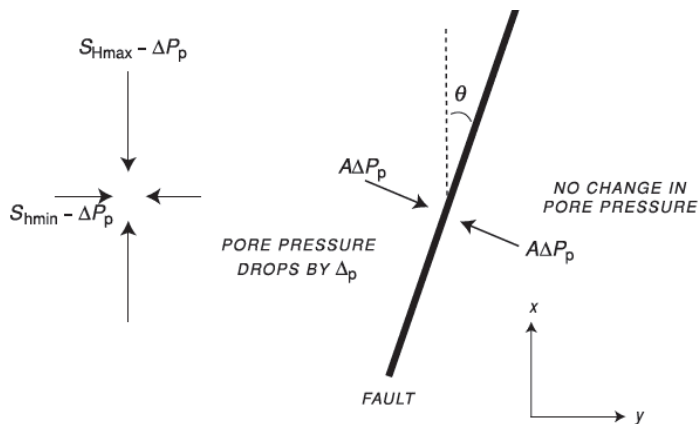


Figure A1: 2D conceptual model for calculating principal stress rotation after isotropic depletion on one side of the fault (Zoback 2010).

The new stress state within the reservoir is:

$$S_x^{new} = (S_{Hmax} - A\Delta Pp) - \frac{1}{2} A\Delta Pp(1 - \cos 2\theta) \quad , \quad (A.1)$$

$$S_y^{new} = (S_{hmin} - A\Delta Pp) - \frac{1}{2} A\Delta Pp(1 + \cos 2\theta) \quad , \quad (A.2)$$

$$S_{xy}^{new} = \pm \frac{1}{2} A\Delta Pp \sin 2\theta \quad . \quad (A.3)$$

The rotation of S_{Hmax} is given by:

$$\gamma = \frac{1}{2} \tan^{-1} \left(\frac{A\Delta Pp \sin 2\theta}{(S_{Hmax} - S_{hmin}) + A\Delta Pp \cos 2\theta} \right) \quad , \quad (A.4)$$

where γ is the rotation, A is the stress path, and θ is the acute angle between S_{Hmax} and the fault plane.

A.2 A general 2D approach

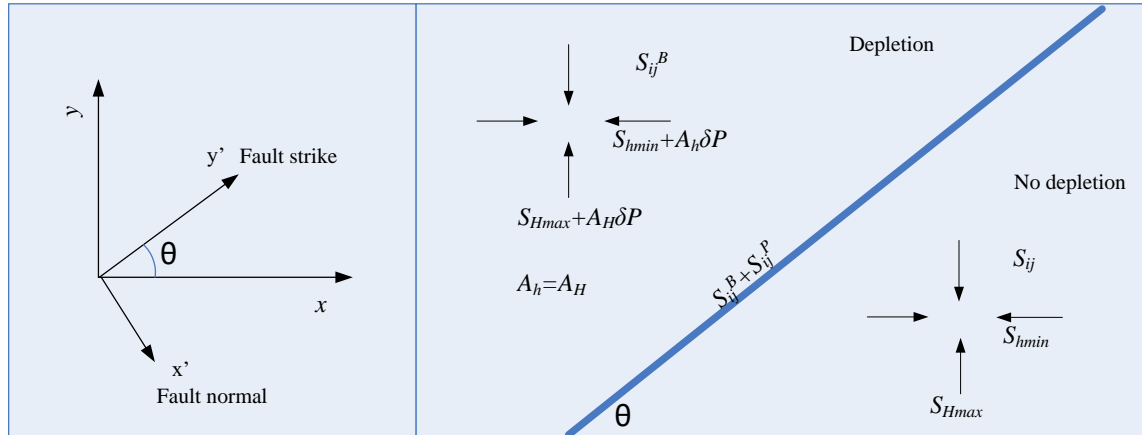


Figure A2: 2D conceptual model for calculating principal stress rotations due to depletion at one side of an impermeable fault

Compared to the original stress state, the depletion induced additional loading is

$$\Delta_{ij} = \begin{bmatrix} A_h \delta p & 0 \\ 0 & A_H \delta p \end{bmatrix} . \quad (\text{A.5})$$

The traction associated with this additional loading is:

$$T_i = \Delta_{ij} n_j = \begin{bmatrix} A_h \delta p & 0 \\ 0 & A_H \delta p \end{bmatrix} \begin{pmatrix} n_x \\ n_y \end{pmatrix} = \begin{pmatrix} A_h \delta p n_x \\ A_H \delta p n_y \end{pmatrix} , \quad (\text{A.6})$$

and the additional normal stress is then:

$$\sigma_n = T_i n_i = A_h \delta p n_x^2 + A_H \delta p n_y^2 . \quad (\text{A.7})$$

If $A_h = A_H = A$, then:

$$\sigma_n = A \delta p , \quad (\text{A.8})$$

and the additional shear stress is 0.

After depletion, assuming $A_h = A_H = A$, the background stress within the reservoir becomes:

$$S_{ij}^B = \begin{bmatrix} S_h + A_h \delta p & 0 \\ 0 & S_H + A_H \delta p \end{bmatrix} = \begin{bmatrix} S_h + A \delta p & 0 \\ 0 & S_H + A \delta p \end{bmatrix} . \quad (\text{A.9})$$

On both sides of the fault, the stress state is perturbed by the depletion-induced normal and shear stresses on the fault. In the case of $A_h = A_H = A$, this perturbation can be found by applying a uniaxial stress perpendicular to the fault and determining the resulting stresses in x-y coordinates. The new stress within the reservoir is a superposition of the background stress and stress perturbation.

The perturbation in the new coordinate system is:

$$S_{i'j'}^p = \begin{bmatrix} S_{x'x'}^p & S_{x'y'}^p \\ S_{y'x'}^p & S_{y'y'}^p \end{bmatrix} = \begin{bmatrix} A \delta p & 0 \\ 0 & 0 \end{bmatrix} . \quad (\text{A.10})$$

Transformed into x-y coordinates, it is:

$$S_{ij}^p = A^T S_{i'j'}^p A \quad , \quad (A.11)$$

where:

$$A = \begin{bmatrix} \cos(x', x) & \cos(x', y) \\ \cos(y', x) & \cos(y', y) \end{bmatrix} = \begin{bmatrix} \cos(\pi/2 - \theta) & \cos(\pi - \theta) \\ \cos \theta & \cos(\pi/2 - \theta) \end{bmatrix} = \begin{bmatrix} \sin \theta & -\cos \theta \\ \cos \theta & \sin \theta \end{bmatrix} \quad . \quad (A.12)$$

Thus:

$$S_{ij}^p = \begin{bmatrix} \frac{1}{2} A \delta p (1 - \cos 2q) & -\frac{1}{2} A \delta p \sin 2q \\ -\frac{1}{2} A \delta p \sin 2q & \frac{1}{2} A \delta p (1 + \cos 2q) \end{bmatrix} \quad . \quad (A.13)$$

The new stress state is:

$$S_{ij}^{new} = S_{ij}^B + S_{ij}^p \quad , \quad (A.14)$$

where the components are:

$$S_x^{new} = (S_h + A \delta p) + \frac{1}{2} A \delta p (1 - \cos(2\theta)) \quad , \quad (A.15)$$

$$S_y^{new} = (S_H + A \delta p) + \frac{1}{2} A \delta p (1 + \cos(2\theta)) \quad , \quad (A.16)$$

$$S_{xy}^{new} = \pm \frac{1}{2} A \delta p \sin(2\theta) \quad . \quad (A.17)$$

The result is consistent with Eq.(A.1)~Eq.(A.3). Note that here, S_{min} is along x direction, and δp is negative for depletion.